Bioconjugate Chemistry

Article

pubs.acs.org/bc

Nano-Confined Squaraine Dye Assemblies: New Photoacoustic and Near-Infrared Fluorescence Dual-Modular Imaging Probes in Vivo

Di Zhang,[†] Ying-Xi Zhao,[†,‡] Zeng-Ying Qiao,[†] Ulrich Mayerhöffer,[§] Peter Spenst,[§] Xiao-Jun Li,[‡] Frank Würthner,*[,§] and Hao Wang*[,†]

[†]CAS Key Laboratory for Biological Effects of Nanomaterials and Nanosafety, National Center for Nanoscience and Technology (NCNST), No. 11 Beiyitiao, Zhongguancun, Haidian District, Beijing, 100190, China

[‡]Hebei University of Technology, No. 8 Guangrongdao, Hongqiao District, Tianjin, 300130, China

[§]Institut für Organische Chemie & Center for Nanosystems Chemistry, Universität Würzburg, Am Hubland, 97074, Würzburg, Germany

Supporting Information

ABSTRACT: For the purpose of near-infrared (NIR) fluorescence and photoacoustic (PA) tomography dual-modular imaging, self-assembly of squaraine (**SQ**) dyes is constructed in the hydrophobic phospholipid bilayers of liposomes (**SQ⊂L**) with variable mixing ratios of **SQ** and phospholipids from 1:500 to 1:10 (w/w). When doping minimal amounts of **SQ**, molecularly dispersed **SQ** in bilayers shows remarkable fluorescence. Interesting, the PA signal is enhanced with increase of **SQ** in the nanoconfined bilayer region, which is attributed to the formation of **SQ**-based *H*-aggregates and enhanced thermal conversion efficiency (η). **SQ⊂L** shows satisfactory chemical and thermal stabilities and photobleaching resistance. **SQ⊂L** is well-distributed in the cytoplasm of MCF-7 cells and its fluorescence signal remains for 7 days without dramatic quenching owing to the good stability of **SQ⊂L**. Furthermore, **SQ⊂L** is subjected to in vivo NIR fluorescence imaging to evaluate the whole-body biodistribution in organ level. Particularly, PA imaging with deeper tissue penetration capability is utilized to investigate the heterogeneous distribution **SQ⊂L** inside solid tumor. The majority of **SQ⊂L** are enriched in the area where the blood vessels are generated, implying that the liposomal nanocarriers exhibit lower tumor tissue penetration capability after the vascular leakage. This result is validated by histological examination of tumor tissue in parallel.

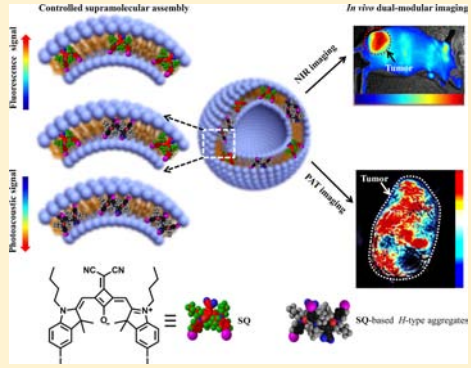

INTRODUCTION

Extensive efforts have been devoted for developing near-infrared (NIR) dyes because of their wide applications in material science, biology, and medicine.[1−5] Since the NIR irradiation was optimal for tissue transmission and low-light Rayleigh-Tyndall scattering, NIR dye-based optical imaging technologies showed substantially enhanced sensitivity and significantly reduced autoabsorption and autofluorescence in vivo.[6,7] However, it is difficult to retrieve pathological information on suborganellar level due to the limited spatial resolution of two-dimensional (2D) NIR imaging technique. In recent years, photoacoustic (PA) tomography technique has emerged as a promising biomedical diagnostic tool due to the higher spatial resolution (1/200 of tested tissue depth) and deeper tissues penetration up to 7 cm capability compared with conventional NIR imaging technique.[8−18] Besides the well-known fluorescence properties of NIR dyes, they can also be utilized as PA contrast agents through conversion of light energy into heat, leading to the transient thermoelastic expansion, and thus launch a wide-band ultrasonic wave.[19−21] Recently, the materials with the higher optical absorption in the NIR range have been successfully demonstrated as PA contrast agents for noninvasive cancer imaging and molecular diagnostics.[11,22,23] However, the "contradictory" design concept for NIR and PA imaging probes greatly hamper the development of the combined imaging technology. NIR imaging probes require high fluorescence quantum yield while PA contrast agents need a high light-to-heat conversion efficiency and a low fluorescence quantum yield. To overcome this problem, we leveraged the two criteria mentioned above by proper adjustment of the self-assembly equilibrium of fluorescence and PA. NIR fluorescence and PA signal readouts can be tuned by controlling of NIR dye packing mode which directly leads to different optical/heating properties. By employing NIR dye assemblies as both NIR and PA imaging probes, we are capable of developing a dual modular imaging platform with high sensitivity, enhanced spatial resolution, and deep tissue penetration in the region of interest (ROI).

Recently, some of us have synthesized a series of dicyanovinyl-functionalized squaraine dyes.[24,25] These accept-

Received: August 25, 2014
Revised: October 4, 2014
Published: November 5, 2014

dx.doi.org/10.1021/bc5003983 | *Bioconjugate Chem.* 2014, 25, 2021−2029

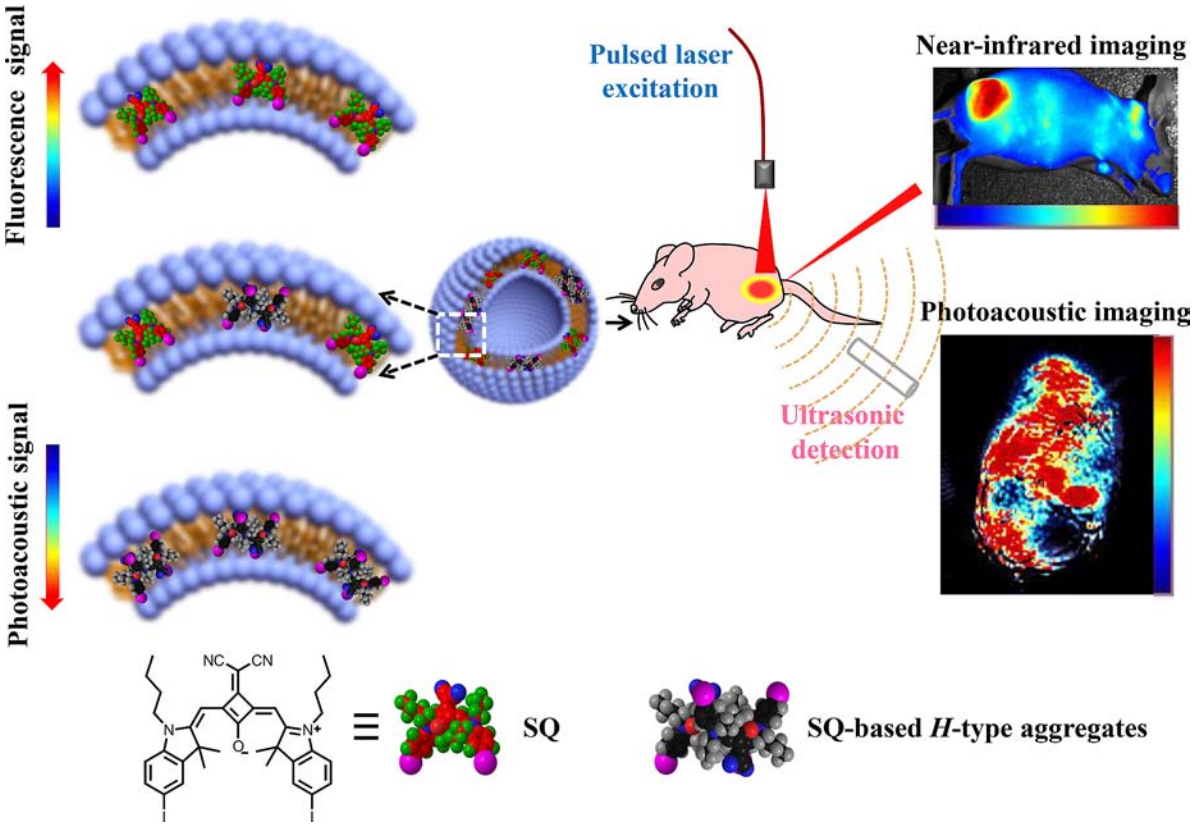

Figure 1. Schematic diagram of the nanoconfined **SQ** assemblies in phospholipid bilayer and the utilization of these vesicles as probes for dual modular tumor imaging in vivo.

or-substituted squaraine dyes not only show superior NIR fluorescence properties (longer absorption wavelength and higher quantum yield), but also exhibit a different, i.e., cisoid, conformation which makes these dyes chemically more robust.[25] Furthermore, we could demonstrate that halogenated derivatives are prone to self-assembly into *H*-aggregates in nonpolar environments[25] and that these aggregates are nonfluorescent in contrast to their monomeric counterparts.[25−29] However, due to the intrinsic hydrophobic properties of these halogenated squaraine dyes, they can only be processed in organic solvents,[24,30] which greatly hampers their application in the biomedical field. Therefore, we expected to explore the new strategy to improve the accessibility of these molecules in aqueous solution. Previously, some of us also showed a self-assembly approach for the preparation of functional supramolecular nanoparticles (SNPs) for biomedical applications.[31−33] By altering the different functional modules, we could tune the size, surface chemistry, and payloads of resulting SNPs and further utilized them for positron emission tomography (PET) imaging, magnetic resonance imaging (MRI), and photothermal cancer treatment.[34−37]

In this work, we demonstrated **SQ**-based self-assembly in nanoconfined hydrophobic phospholipid bilayers of liposomes and the utilization of such functional liposomes for NIR and PA dual-modular imaging in vivo (Figure 1). The reversible self-assembly of **SQ** monomers into *H*-type aggregates could be adjusted in the hydrophobic bilayers by simply altering the mixing ratio of **SQ** and phospholipid. The monomer and *H*-type aggregates of **SQ** contributed to the resulting of NIR fluorescence and PA signals, respectively. The fluorescence quenching with formation of aggregates leads to the thermal release after laser irradiation.[12] It is well-known that the generation of PA signals is directly related to the thermal expansion which is closely related to the thermal conversion efficiency (η). Therefore, the higher mixing ratio of **SQ** in liposome formed *H*-type aggregates exhibiting higher η, further leading to much stronger PA signal. After optimization of the molecular composition, the **SQ**-embedded liposome (**SQ⊂L**) could serve as a stable and biocompatible nanoprobe for NIR and PA dual modular imaging with high sensitivity, enhanced spatial resolution, and deep tissue penetration. **SQ⊂L** showed satisfactory chemical and thermal stability in physiological condition and high antiphotobleaching ability compared to the commercially available Cy-5 dye. The biodistribution of **SQ⊂L** was determined rapidly by whole-body NIR imaging. The heterogeneous distribution of **SQ⊂L** in targeted tumor was further carefully investigated by conjunction of three-dimensional (3D) PA imaging with higher spatial resolution.

RESULTS AND DISCUSSION

Preparation and Characterization of SQ⊂L. Liposomes have been widely applied as drug delivery vehicles to enhance drug solubility and bioavailability.[38−40] Accordingly, this well-defined hydrophobic bilayer should also be suitable for the accommodation of hydrophobic squaraine dyes. Furthermore, the hydrophobic aliphatic interior of liposomes was expected to provide an ideal environment to promote self-assembly of **SQ** into *H*-aggregates, similarly to our previous work in nonpolar solvents.[41] With this idea in mind, we prepared **SQ** self-assemblies confined in liposomes by the ethanol injection method.[42,43] Briefly, L-α-phosphatidylcholine and cholesterol (4:1 w:w) were dissolved in the ethanol solution. Afterward, the

dx.doi.org/10.1021/bc5003983 | *Bioconjugate Chem.* 2014, 25, 2021−2029

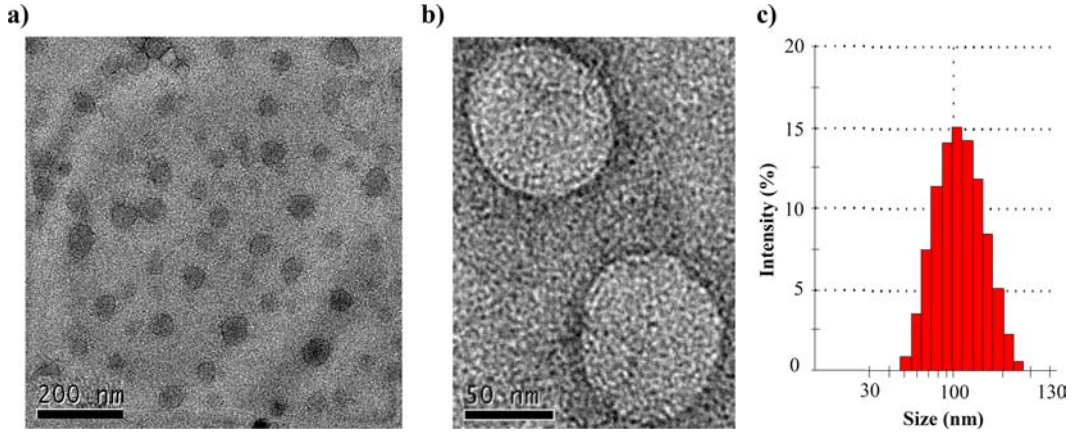

Figure 2. (a, b) TEM images of **SQ⊂L** with different magnifications; (c) hydrodynamic size of **SQ⊂L** recorded in PBS by using DLS.

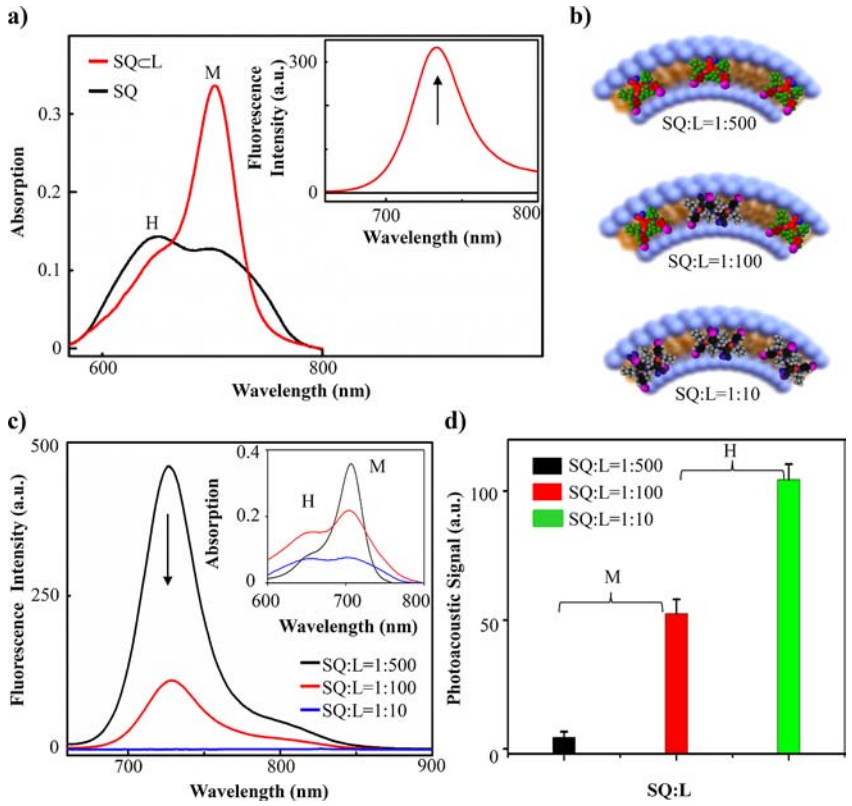

Figure 3. (a) UV/vis absorption spectra and the corresponding fluorescence intensity changes (inset, λ_{ex}: 680 nm) of aggregated **SQ** (4 μM) in PBS and **SQ** monomers (4 μM) in **SQ⊂L**. (b) Cartoon illustration of controlled supramolecular assembly mode of **SQ** in phospholipid bilayer. (c) Fluorescence intensity (λ_{ex}: 680 nm) changes of **SQ** (2.5 μM) with variable mixing ratios of phospholipids from 1:500 to 1:10 (w/w) and the corresponding UV/vis absorption spectral changes (inset). (d) PA signal was enhanced with increasing ratio of **SQ** and phospholipid in liposomes from 1:500 to 1:10 (w/w). Error bar in (d) represented the SD of experimental duplicates. H and M represent the *H*-type aggregates and monomer, respectively.

SQ containing DMSO solution was added into the above-mentioned premixed ethanol solution. The resulting mixture was subsequently injected into phosphate-buffered saline (PBS) and kept stirring for 1 h during which the **SQ** molecules preferentially embedded into hydrophobic phospholipid bilayer of liposome through hydrophobic interaction. The morphology of **SQ⊂L** in PBS (pH = 7.4) was investigated by transmission electron microscope (TEM). Under the ratio (1:500) of **SQ** and phospholipids, uniformed vesicular structures of **SQ⊂L** with a size of 76 ± 15 nm were observed (Figure 2a and b). Dynamic light scattering (DLS) result showed a hydrodynamic diameter of **SQ⊂L** of 103 ± 14 nm with narrow size distribution (PDI: 0.18, Figure 2c).

Optical Properties of SQ⊂L. The UV/vis and fluorescence spectra of **SQ** in DMSO/H_2O mixing solutions were studied and results[44] are shown in Supporting Information, Figure S1. Accordingly, for water content of <40% monomeric and fluorescent **SQ** prevailed, while at higher water content **SQ** was in the aggregated nonfluorescent state. However, when **SQ** was embedded in liposome (**SQ⊂L**), a strong fluorescence was observed at low **SQ** content compared to their nonfluorescent *H*-type aggregates of **SQ** at the same concentration in aqueous

dx.doi.org/10.1021/bc5003983 | *Bioconjugate Chem.* 2014, 25, 2021−2029

environment (Figure 3a). This turn-on fluorescence was attributed to the liberation of monomeric **SQ** dyes within the better solvating hydrophobic environment of the bilayer membrane. Nevertheless, the fluorescence of **SQ⊂L** was again reduced and finally entirely quenched with increase of the ratio of **SQ** and phospholipid from 1:500 to 1:10 (w/w) (Figure 3b,c). From the UV/vis absorption spectra (inset in Figure 3c), we deduced that **SQ** self-assembled in the nanoconfined liposomes from monomer to aggregates, similar to the conventional self-assembly processes in solution. Concomitantly the PA signals of **SQ⊂L** enhanced with an increase in the amount of **SQ** up to 10 times from 1:500 to 1:10 mixing ratio (Figure 3d). Meanwhile, the hydrodynamic diameter and PDI of **SQ⊂L** were insignificant changed with enhanced ratios of **SQ** and phospholipid from 1:500 to 1:10 (see Supporting Information, Figure S2). For the purpose of dual-modular imaging, we chose **SQ⊂L** (1:100 w:w) as optimal imaging nanoprobes for our further experiments.

Photothermal Transformation of SQ⊂L. The PA signal is proportional to the thermal conversion efficiency (η) of the substrates.[45,46] To understand the mechanism of PA signal enhancement of **SQ⊂L**, we first measured the η values of **SQ⊂L** with different mixing ratios of **SQ** in liposomes. The photothermal transduction photographs were obtained through the thermal camera (America, FLIR E60: thermal sensitivity: 0.05 °C; range of temperature: −20−650 °C) to monitor the temperature changes (see Supporting Information, Figure S3). The temperature of the **SQ⊂L** solutions were increased and rapidly reached maximum in 1 min with increase of **SQ**. The time-dependent temperature heating/cooling curves were showed in Supporting Information, Figure S4. The highest temperature of the solutions with mixing ratios of **SQ** in liposomes (i.e., 1:500, 1:100, and 1:10, w/w) was 38, 50, and 68 °C, respectively (Table 1). The time constant for heat transfer

Table 1. Values of the Photothermal Transduction Parameters of SQ⊂L with Different Ratios of SQ:Phospholipids in Liposomes

SQ:phospholipids	T_{max}	T_{surr}	τ_s (s)	r^2	η (%)
1:500	38	23.6	83	0.9957	10
1:100	50	23.5	75	0.9976	46
1:10	68	23.3	60	0.9978	63

from the system was determined to be τ_s (s) by applying the linear time data from the cooling time after 120 s (see Supporting Information, Figure S5). The values of τ_s at the above three formulations were 83, 75, and 60 s, respectively (Table 1). From eqs 1−4 (see Experimental Section),[47] the η values of **SQ⊂L** were 10%, 46%, and 63% with the tendency to form aggregates (Table 1). The η value of aggregated **SQ** was 6.3-fold enhanced compared to that of free **SQ** in liposomes. All together, the higher thermal conversion efficiency of the solution **SQ⊂L** with aggregated **SQ** molecules versus free ones contributed to the enhanced PA signal intensity of PA agents.

Stability of SQ⊂L. To evaluate the photostability of **SQ⊂L**, the antiphotobleaching property of **SQ⊂L** was investigated in comparison to the most commonly used fluorescent NIR dye Cy-5[48] and Nile red. First, the same absorption solution of **SQ⊂L** and Cy5 (see Supporting Information, Figure S6) was placed in quartz tubes for continuous laser irradiation, separately (Cy-5, λ_{ex}: 630 nm, λ_{em}: 660 nm; **SQ⊂L**, λ_{ex}: 680 nm, λ_{em}: 733 nm). The time-dependent fluorescence changes of **SQ⊂L** and Cy-5 were shown in Figure S7. After illumination of **SQ⊂L** for 1200 s, no variation in fluorescence intensity was observed of **SQ⊂L**. In contrast, the fluorescence intensity of Cy-5 dye decayed more than 20% from 0 to 500 s, consistent with a higher photobleaching rate. Meanwhile, the fluorescence changes of solution of Nile red⊂L and **SQ⊂L** was also investigated (see Supporting Information, Figures S8, 9, and 10). From the results of normalized the fluorescence intensity change (see Supporting Information, Figure S11), we can see that the stability of **SQ⊂L** can be compared with the stability Nile red⊂L.

The higher photostability of **SQ⊂L** was attributed to the inert properties of **SQ** molecules within the hydrophobic environment of liposome. In addition, the chemical and physiological condition stability of **SQ⊂L** was also studied. First, the chemical stability was investigated through coincubation of **SQ⊂L** and glutathione (GSH), which is one of the most abundant nucleophilic biomolecules in nature, for 90 min in PBS; the fluorescence intensity of **SQ⊂L** remained unchanged (Figure S12). Then, the stability of the **SQ⊂L** in physiological condition was studied by addition of the bovine serum albumin (BSA, 5%) in the solution of **SQ⊂L**. The time-dependent UV/vis absorption and fluorescence intensity changes (see Supporting Information, Figures S13 and 14) showed that **SQ⊂L** can stably exist in the physiological condition for at least 36 h. Meanwhile, the hydrodynamic diameters of **SQ⊂L** were insignificantly changed after incubation with BSA (5%) for 36 h (see Supporting Information, Figure S15). The thermal stability was also investigated at physiological temperature. We did not observe variations of the fluorescence intensity of **SQ⊂L** at 37 °C (see Supporting Information, Figure S16). Altogether, **SQ⊂L** not only had strong stability in physiological condition, but could also resist attack by strong biological nucleophiles.

NIR Fluorescence Properties of SQ⊂L in Vitro. To investigate the NIR fluorescence properties of **SQ⊂L** in vitro, we incubated **SQ⊂L** and free **SQ** with MCF-7 cells for 4 h, and then the fluorescence of MCF-7 cells was monitored through confocal laser scan microscopy. As shown in Figure 4, **SQ⊂L** exhibited high fluorescence intensity and uniformed distribution in the cytoplasm of cells. The intracellular **SQ⊂L** signals remained after 7 days, indicating the long-term imaging possibility of **SQ⊂L**. In contrast, weak and heterogenous fluorescence of **SQ** in the absence of liposomes was observed in cells. In addition, the cytotoxicity assay of **SQ⊂L** and free **SQ** was conducted by incubation with MCF-7 cells, and negligible cytotoxicity was observed after 24 h (see Supporting Information, Figure S17).

Tumor Imaging in Vivo. The whole body distributions of **SQ⊂L** and free **SQ** in tumor-bearing mice were studied by NIR fluorescence imaging technique. BALB/c nude female mice were obtained from the Department of Laboratory Animal Science, Peking University Health Science Center, and all animal experiments were conducted by its center. Animals were maintained in the center for experimental animals (an AAALAC-accredited experimental animal facility).

All procedures involving experimental animals were performed in accordance with protocols approved by the Committee for Animal Research of Peking University, China. MCF-7 cells (5×10^6) in PBS (100 μL) solution were subcutaneously injected into the right flank of BALB/c nude mice. The initial body weight of mice was about 18−19 g. After 3 weeks of tumor formation, **SQ⊂L** (60 μM calculated based

dx.doi.org/10.1021/bc5003983 | Bioconjugate Chem. 2014, 25, 2021−2029

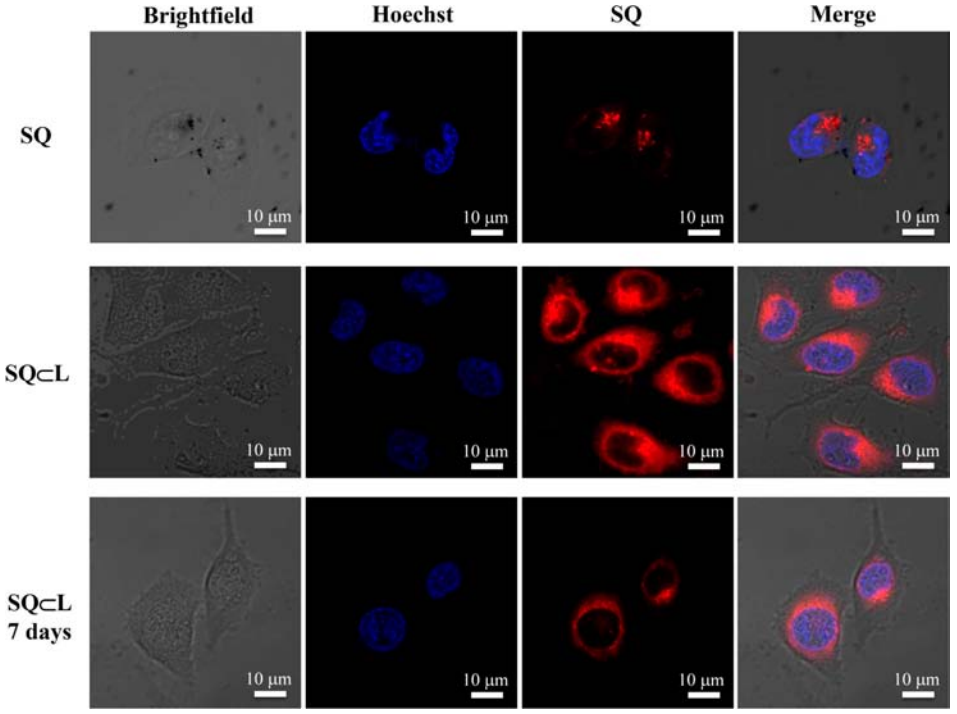

Figure 4. Fluorescence confocal microscopic images of MCF-7 cells treated with free **SQ** (10 μM) and **SQ⊂L** (10 μM) for 4 h: the fluorescence of **SQ⊂L** can be maintained for 7 days in MCF-7 cells (**SQ** and **SQ⊂L**, emission at 633 nm). The nuclei of cells were stained with Hoechst 33342 (emission at 405 nm) exhibiting blue fluorescence.

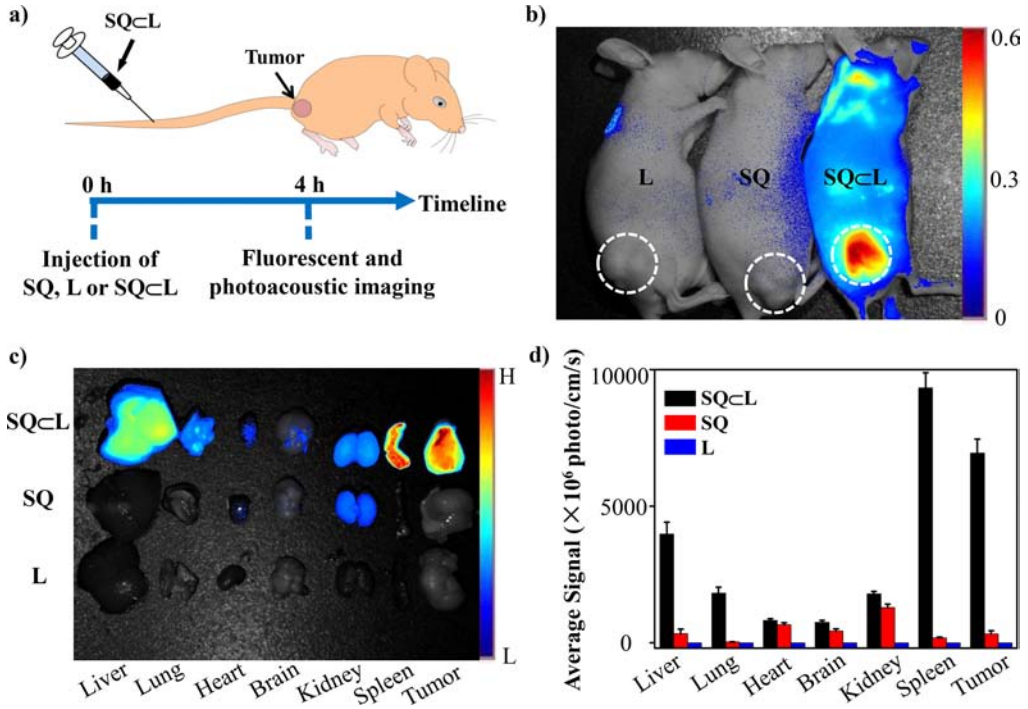

Figure 5. (a) Schematic treatment protocol of the mice by **SQ**, **SQ⊂L**, and liposome. **SQ**, **SQ⊂L**, and liposome (5 mg/kg of liposome content) were intravescularly injected into BALB/c nude mice bearing MCF-7 tumor, and images were acquired 4 h post-administration of **SQ⊂L** and the controls. (b) In vivo NIR optical image of mice (white circles indicate the tumor). (c) Ex vivo image and the average signal intensities of major organs, i.e., liver, lung, heart, brain, kidney, spleen, and tumor. (d) Quantitative fluorescence signal distribution of **SQ⊂L** and controls in major organs; each column represents the mean value (N = 3).

on the **SQ** content, 200 μL), **SQ** (60 μM, 200 μL), and liposome vehicles were intravenous injected into mice through tail vein (N = 3). We next performed NIR imaging after 4 h administration of probes following the timeline shown in Figure 5a. For the group treated with **SQ⊂L** for 4 h, significant accumulation of **SQ⊂L** in tumor was observed (Figure 5b). Six-fold increase in average pixel intensity was observed compared with that of control groups in tumor, while there was no

dx.doi.org/10.1021/bc5003983 | *Bioconjugate Chem.* 2014, 25, 2021−2029

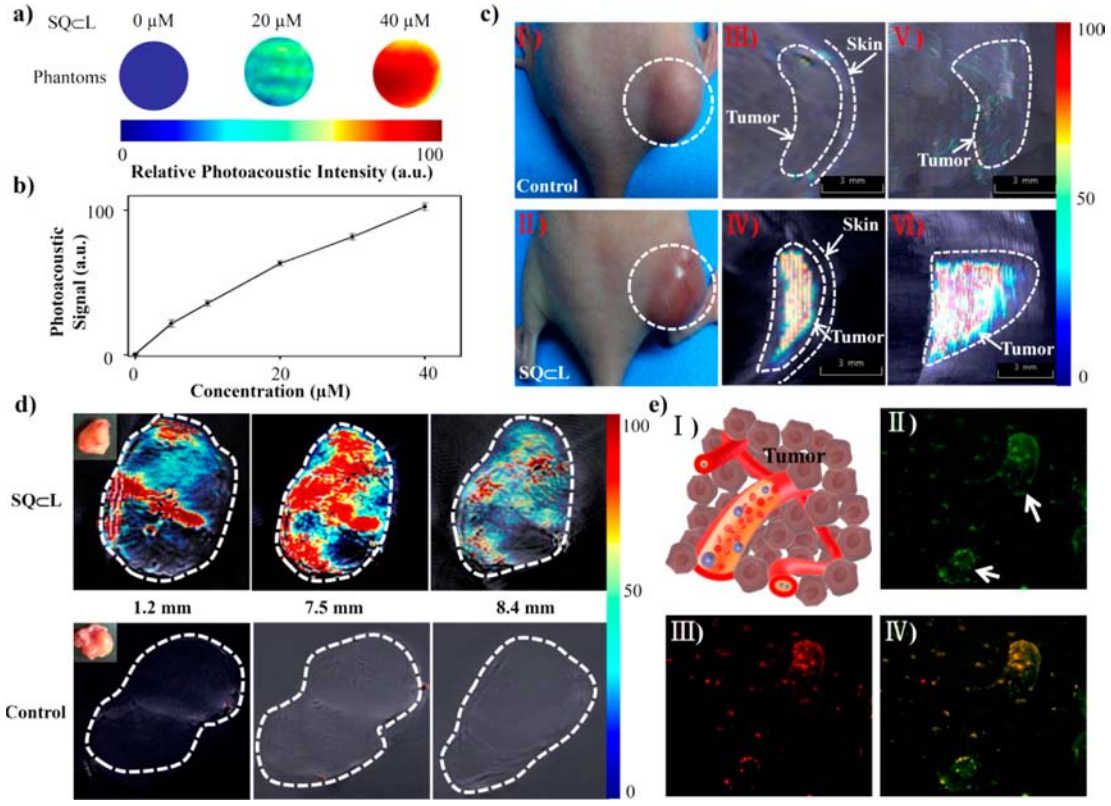

Figure 6. (a) PA images of **SQ⊂L** (0, 20, and 40 μM) in agarose phantoms. (b) Concentration-dependent PA signal changes of **SQ⊂L**. (c) PA imaging of tumor in MCF-7 xenografted mice: (I) and (II) are the representative photos of tumor bearing mice with different treatments; (III) and (IV) show one transverse slice in the 3D PA image of tumor bearing mice with treatment of liposome and **SQ⊂L**. The dashed line and the white dashed circle indicate the skin and outlines of tumor site of mice, respectively; (V) and (VI) show the aligned images from the different transverse section of control and treated groups. (d) Tumor was dissected after the PA imaging of tumor bearing mice: the signal-to-depth photos and the relative PA images of ex vivo tumor treated by **SQ⊂L** and liposome with different depth at 1.2, 7.5, and 8.4 mm, respectively. (e) Heterogeneous suborganellar distribution of **SQ⊂L** in solid tumor: (I) illustration of **SQ⊂L** accumulation in blood vessels of tumor; (II) immunohistochemical stained section of tumor and blood vessels were stained by a cluster of differentiation 31 (CD31, anti-CD31 antibodies IgG labeled by FITC, green); (III) fluorescence of **SQ⊂L** (red) distributed in tumor; and (IV) merged picture of green and red. Error bar in (b) represents the SD of experimental duplicates.

fluorescence signal in the corresponding tumor of control mice receiving **SQ** injection, which may be caused by the short blood circulation time and fast body clearance rate of **SQ** molecules in vivo. To quantitatively study the whole-body biodistribution of **SQ⊂L**, the animals were sacrificed, and then tumor, heart, liver, spleen, lung, brain, and kidney were excised for fluorescent imaging. All images were analyzed and collected with the Maestro In-Vivo imaging system equipped with a 680/40 nm band-pass filter for excitation and a 725 nm long-pass filter for emission. As shown in Figure 5c and d, **SQ⊂L** accumulated primarily in the spleen (9336×10^6 photo cm^{-2} s^{-1}), tumor (6950×10^6 photo cm^{-2} s^{-1}), and liver (3980×10^6 photo cm^{-2} s^{-1}), which was probably attributed to the mononuclear phagocyte uptake[49,50] and enhanced permeability and retention (EPR) effect of **SQ⊂L**. The stronger NIR signal and higher distribution of **SQ⊂L** in tumor was a result of the longer lifetime in blood circulation and accumulation in the tumor site by the enhanced EPR effect. There were no fluorescence signals observed in major organs except for the kidney with weak fluorescence upon administration of free **SQ** molecules. One reasonable explanation is that the **SQ** molecule was quickly expelled from the body through the kidney pathway. Given that the delivery of cargo to different tumor microenvironments will directly affect their imaging quality and/or therapeutic efficacy,[51] we attempted to employ the PA technique with higher spatial resolution to monitor the heterogeneous **SQ⊂L** distribution in tumor tissue. First, we verified the effectiveness of **SQ⊂L** as PA imaging contrast agent in vitro. We injected **SQ⊂L** and a control group in the agarose phantoms (2% agarose power was dissolved in water) to mimic the tumor tissue. By adding different concentrations of **SQ⊂L** (0–40 μM) in agarose phantoms, we examined the concentration-dependent PA performance of **SQ⊂L**. The representative PA imaging with concentrations of **SQ⊂L** (0, 20, and 40 μM) in phantoms is shown in Figure 6a. Apparently, the PA signals surged with increase of the concentrations of **SQ⊂L** from 0 to 40 μM. No PA signals of liposomes were detected under the same conditions. The profile of relative PA signals versus concentrations of **SQ⊂L** is shown in Figure 6b.

We then performed the PA imaging of tumor-bearing mice (Figure 6c I and II) with administration of **SQ⊂L** and liposome. Four hours after **SQ⊂L** and liposome injection, the mice were scanned with a photoacoustic imaging instrument (mode: Multispectral Optoacoustic Tomography: MSOT 128, Cold Spring Biotech Corp., excitation wavelength at 680 ± 1 nm, pulse frequency with 10 Hz, sound speed: 1). Then, a series of 2D images were recorded. The 3D imaging was acquired through combining the 2D images. The transverse sections of 3D PA images were shown in Figure 6c III and IV. Ten-fold enhancement of PA signals was detected in tumors of

dx.doi.org/10.1021/bc5003983 | *Bioconjugate Chem.* 2014, 25, 2021–2029

mice treated with **SQ⊂L** compared with that of groups only treated with liposome. The outline of the tumor was clearly observed after alignment with all of the transverse sections of mice treated with **SQ⊂L**. However, it was difficult to distinguish the tumor sites of mice only treated with liposome (Figure 6c V and VI).

We performed ex vivo 3D PA imaging of solid tumor with 0.3 mm in-depth scan per section. The average PA signal in tumors treated with **SQ⊂L** was higher than that of the control group. Interestingly, we noticed that the PA signal did not show the signal-to-depth rule if the distribution was homogeneous, i.e., the PA signals decayed with increase of the tissue depth. In our case, the PA signal was enhanced when we scanned the solid tumor from the exterior to the interior. As can be seen from Figure 6d and Supporting Information Figure S18, the **SQ⊂L** was mainly distributed heterogeneously in the interior of the solid tumor. Considering that the **SQ⊂L** was accumulated in the tumor by the EPR effect, we deduced that the major pathway for **SQ⊂L** transportation in the tumor was new blood vessels upon the transition of tumor from a benign state to a malignant one. To validate this hypothesis, we stained the blood vessels with clusters of differentiation 31 (CD31, anti-CD31 antibodies IgG labeled by FITC, green) in tumor tissue slides and examined the colocalization of the **SQ⊂L** fluorescence signal (red) with blood vessel ones. The nice overlap of green and red signals indicated that the **SQ⊂L** was mainly accumulated in the newly developed blood vessels in tumor (Figure 6e).

In conclusion, the near-infrared fluorescence and photoacoustic tomography imaging in vivo show great potential in preclinical investigations. We leveraged the two criteria mentioned by proper adjustment of the self-assembly equilibrium of fluorescent and PA of **SQ** monomer and **SQ** *H*-aggregates in the nanoconfined hydrophobic bilayers of liposomes by altering the mixing ratio of **SQ** and phospholipid. The monomer and *H*-aggregate of **SQ** contribute to the resulting NIR fluorescence and PA signal, respectively, and enhancement of the PA signal was caused by increasing the η after formation of *H*-aggregates in the nanoconfined hydrophobic bilayers. The optimized **SQ⊂L** can serve as a stable and biocompatible nanoprobe for NIR and PA dual modular imaging with high sensitivity, enabled rapid whole-body scan, and enhanced spatial resolution and deep tissue penetration. We envision that the conjunction of **SQ⊂L** with dual-signal readouts of NIR and PA imaging techniques will show much broader potential in preclinical studies.

EXPERIMENTAL PROCEDURES

UV/vis Absorption and Fluorescence of SQ and SQ⊂L. The **SQ** was dissolved in dimethyl sulfoxide (DMSO) with the concentration of 2500 μM. In the UV/vis (wavelength range: 500−800 nm, slit width: 1.0 nm, measurement mode: absorption) absorption study, the concentration of **SQ** was diluted to 4 μM with different ratio of DMSO and PBS (0−99% water). The fluorescence intensity of **SQ** at the same ratio of DMSO and PBS was measured with the excitation wavelength at 680 nm, and the emission wavelength at 733 nm with fluorescence spectrometer. The fluorescence of **SQ⊂L** was measured in the PBS solution, and the other conditions were the same with the condition of monomer **SQ**.

TEM of the SQ⊂L and Liposomes. The samples of TEM were prepared by drop-coating 2 μL of the solution with **SQ⊂L** and liposomes, respectively, onto carbon-coated copper grids. After 1 min, the solution was removed with filter paper. Then the sample was stained for 25 s by a solution of uranium acetate. Finally, the morphological changes of **SQ⊂L** and liposomes were examined by TEM (model: Tecnai G2 20 S-TWIN). The hydrodynamic diameter of liposomes was also measured by using Zetasizer Nano ZS (Malvern Instruments Ltd.).

Thermal Conversion Efficiency of SQ⊂L. **SQ⊂L** (50 μM, 0.05 mL) was injected into the cap of the centrifuge tube and irradiated with laser (λ_{ex} = 700 nm, 0.22 W/cm^2, 80 MHz, 100 fs, titanium sapphire femtosecond laser with 4 mm diameter of facula). Following the previously reported methods, the value of η can be calculated from the following equations:

$$\eta = [hS(T_{max} - T_{surr}) - Q_{dis}]/I(1 - 10^{-A700}) \quad (1)$$

$$hS = \sum_i m_i C_{p,i}/\tau_s \quad (2)$$

$$t = -\tau_s \ln \theta \quad (3)$$

$$\theta = (T - T_{surr})/(T_{max} - T_{surr}) \quad (4)$$

where I was laser power (0.22 W/cm^{-2}), $A700$ was the absorption of **SQ⊂L** at 700 nm ($A700$ = 5.3), T_{max} were T_{surr} was the temperature of maximum and surroundings (°C), t was the time of cooling process after shutting off the laser (0−120 s), m_i was the mass of the solution, Cp,i was the heat capacity (4.2 J/g °C), and τ_s was the time constant (s). The time-dependent changes of θ were shown in Supporting Information Figure S19.

Cytotoxicity Assay. MCF-7 cells (5×10^4 cells per well) at the logarithmic growth phase were incubated in 96-well culture plates for 17 h with DMEM supplemented with 10% FBS, 1% penicillin and streptomycin at 37 °C in humidity and 5% CO_2 atmosphere, and the culture medium was then replaced by fresh DMEM. Then, different concentration of **SQ⊂L** and **SQ** were added into the fresh culture medium cultured with MCF-7 cells, respectively. The supernatant was removed and washed with PBS twice after 24 h incubation at 37 °C in humidity and 5% CO_2 atmosphere, and then 200 μL of fresh culture medium supplemented with 10% FBS (fetal bovine serum) and 1% penicillin and streptomycin were added into the wells. Subsequently, the solution of CCK-8 (20 μL) was added to the wells followed by 4 h incubation at 37 °C in humidity and 5% CO_2 atmosphere. Finally, the absorbance values of the cells per well were determined with a Microplate Reader at 450 nm for analyzing cell viability. Control experiments were done with addition of the same volume of PBS alone, and the other treatments were under the same condition.

The cell viability was calculated by the equation as follows:

$$\text{cell viability} = A_s/A_c \times 100\% \quad (5)$$

where the A_s was the absorbance of the different treatments with **SQ⊂L** and **SQ** and A_c was the absorbance of the control treatment with PBS.

Confocal Laser Scanning Microscopy. MCF-7 cells (1×10^5) were incubated in the confocal dish with DMEM supplemented with 10% FBS, 1% penicillin and streptomycin at 37 °C in humidity and 5% CO_2 atmosphere. The culture medium was replaced by medium without FBS after 17 h incubation, and then the fluorescent probe (10 μM) of **SQ⊂L** and **SQ** was added into the medium, respectively. The medium was removed after 4 h incubation and then washed with PBS

dx.doi.org/10.1021/bc5003983 | *Bioconjugate Chem.* 2014, 25, 2021−2029

three times. The cells were also stained with Hoechst 33342 for 10 min and washed three times with PBS and the cells kept in PBS. Laser scanning confocal microscopy (LSM710META, Zeiss, Germany, **SQ⊂L** and **SQ** excitation at 633 nm and Hoechst 33342 excitation at 405 nm) was used to investigate the internalization of dyes, and the stability of the fluorescence of **SQ⊂L** in cells was investigated by immobilizing the cell with 4% glutaraldehyde and then the stability of **SQ⊂L** in cells obtained after 7 days.

PA Imaging in Phantom. Different concentrations of **SQ⊂L** were added into the agarose tube with the liposome counterpart as control. The concentrations of **SQ⊂L** were 0, 5, 10, 20, 30, and 40 μM. The phantom was scanned by photoacoustic imaging (MOST 128, iTheraMedical, Germany) and the PA signal intensity was recorded through mean pixel intensity of the same area of the images with the same intensity of laser pulse.

■ ASSOCIATED CONTENT

Supporting Information

Materials, preparation of nanoparticles, stability **SQ⊂L**, Figures S1−S19. This material is available free of charge via the Internet at http://pubs.acs.org.

■ AUTHOR INFORMATION

Corresponding Authors

*E-mail: wanghao@nanoctr.cn.
*E-mail: wuerthner@chemie.uni-wuerzburg.de.

Author Contributions

Di Zhang and Ying-Xi Zhao contributed equally to this work.

Notes

The authors declare no competing financial interest.

■ ACKNOWLEDGMENTS

This work was supported by the National Basic Research Program of China (973 Program, 2013CB932701) and the 100-Talent Program of the Chinese Academy of Science (Y2462911ZX), National Natural Science Foundation (21374026, 21304023 and 51303036), and Beijing Natural Science Foundation (2132053).

■ REFERENCES

(1) Frangioni, J. V. (2003) *In vivo* near-infrared fluorescence imaging. *Curr. Opin. Chem. Biol. 7*, 626−634.

(2) Sun, H. T., Hosokawa, A., Miwa, Y., Shimaoka, F., Fujii, M., Mizuhata, M., Hayashi, S., and Deki, S. (2009) Strong ultra-broadband near-infrared photoluminescence from bismuth-embedded zeolites and their derivatives. *Adv. Mater. 21*, 3694−3698.

(3) Chen, J., Tao, J., Ban, D., Helander, M. G., Wang, Z., Qiu, J., and Lu, Z. (2012) Hybrid organic/inorganic optical up-converter for pixel-less near-infrared imaging. *Adv. Mater. 24*, 3138−3142.

(4) Zhang, Z., Wang, J., and Chen, C. (2013) Near-infrared light-mediated nanoplatforms for cancer thermo-chemotherapy and optical imaging. *Adv. Mater. 25*, 3869−3880.

(5) Luo, S., Zhang, E., Su, Y., Cheng, T., and Shi, C. (2011) A review of NIR dyes in cancer targeting and imaging. *Biomaterials 32*, 7127−7138.

(6) Hilderbrand, S. A., and Weissleder, R. (2010) Near-infrared fluorescence: application to *in vivo* molecular imaging. *Curr. Opin. Chem. Biol. 14*, 71−79.

(7) Feng, L., Wu, L., and Qu, X. (2013) New horizons for diagnostics and therapeutic applications of graphene and graphene oxide. *Adv. Mater. 25*, 168−186.

(8) Wang, L. V., and Hu, S. (2012) Photoacoustic tomography: *in vivo* imaging from organelles to organs. *Science 335*, 1458−1462.

(9) Zerda, A. D. L., Zavaleta, C., Keren, S., Vaithilingam, S., Bodapati, S., Liu, Z., Levi, J., Smith, B. R., Ma, T. J., Oralkan, O., Cheng, Z., Chen, X., Dai, H., Khuri Yakub, B. T., and Gambhir, S. S. (2008) Carbon nanotubes as photoacoustic molecular imaging agents in living mice. *Nat. Nanotechnol. 3*, 557−562.

(10) Xu, M. H., and Wang, L. V. (2006) Photoacoustic imaging in biomedicine. *Rev. Sci. Instrum. 77*, 041101−041122.

(11) Dragulescu Andrasi, A., Kothapalli, S. R., Tikhomirov, G. A., Rao, J., and Gambhir, S. S. (2013) Activatable oligomerizable imaging agents for photoacoustic imaging of furin-like activity in living subjects. *J. Am. Chem. Soc. 135*, 11015−11022.

(12) Lovell, J. F., Jin, C. S., Huynh, E., Jin, H., Kim, C., Rubinstein, J. L., Chan, W. C. W., Cao, W., Wang, L. V., and Zheng, G. (2011) Porphysome nanovesicles generated by porphyrin bilayers for use as multimodal biophotonic contrast agents. *Nat. Mater. 10*, 324−332.

(13) Akers, W. J., Kim, C., Berezin, M., Guo, K., Fuhrhop, R., Lanza, G. M., Fischer, G. M., Daltrozzo, E., Zumbusch, A., Cai, X., Wang, L. V., and Achilefu, S. (2011) Noninvasive photoacoustic and fluorescence sentinel lymph node identification using dye-loaded perfluorocarbon nanoparticles. *ACS Nano 5*, 173−182.

(14) de la Zerda, A., Bodapati, S., Teed, R., May, S. Y., Tabakman, S. M., Liu, Z., Khuri-Yakub, B. T., Chen, X., Dai, H., and Gambhir, S. S. (2012) Family of enhanced photoacoustic imaging agents for high-sensitivity and multiplexing studies in living mice. *ACS Nano 6*, 4694−4701.

(15) Cook, J. R., Frey, W., and Emelianov, S. (2013) Quantitative photoacoustic imaging of nanoparticles in cells and tissues. *ACS Nano 7*, 1272−1280.

(16) Hannah, A., Luke, G., Wilson, K., Homan, K., and Emelianov, S. (2013) Indocyanine green-loaded photoacoustic nanodroplets: dual contrast nanoconstructs for enhanced photoacoustic and ultrasound imaging. *ACS Nano 8*, 250−259.

(17) Nie, L., Chen, M., Sun, X., Rong, P., Zheng, N., and Chen, X. (2014) Palladium nanosheets as highly stable and effective contrast agents for in vivo photoacoustic molecular imaging. *Nanoscale 6*, 1271−1276.

(18) Cheng, L., Liu, J., Gu, X., Gong, H., Shi, X., Liu, T., Wang, C., Wang, X., Liu, G., Xing, H., Bu, W., Sun, B., and Liu, Z. (2014) PEGylated WS2 nanosheets as a multifunctional theranostic agent for in vivo dual-modal CT/photoacoustic imaging guided photothermal therapy. *Adv. Mater. 26*, 1886−1893.

(19) Homan, K. A., Souza, M., Truby, R., Luke, G. P., Green, C., Vreeland, E., and Emelianov, S. (2011) Silver nanoplate contrast agents for *in vivo* molecular photoacoustic imaging. *ACS Nano 6*, 641−650.

(20) Ku, G., Zhou, M., Song, S., Huang, Q., Hazle, J., and Li, C. (2012) Copper sulfide nanoparticles as a new class of photoacoustic contrast agent for deep tissue imaging at 1064 nm. *ACS Nano 6*, 7489−7496.

(21) Jokerst, J. V., Cole, A. J., Van de Sompel, D., and Gambhir, S. S. (2012) Gold nanorods for ovarian cancer detection with photoacoustic imaging and resection guidance via raman imaging in living mice. *ACS Nano 6*, 10366−10377.

(22) Huynh, E., Jin, C. S., Wilson, B. C., and Zheng, G. (2014) Aggregate enhanced trimodal porphyrin shell microbubbles for ultrasound, photoacoustic, and fluorescence imaging. *Bioconjugate Chem. 25*, 796−801.

(23) Ng, K. K., Shakiba, M., Huynh, E., Weersink, R. A., Roxin, Á., Wilson, B. C., and Zheng, G. (2014) Stimuli-responsive photoacoustic nanoswitch for in vivo sensing applications. *ACS Nano 8*, 8363−8373.

(24) Mayerhöffer, U., Gsänger, M., Stolte, M., Fimmel, B., and Würthner, F. (2013) Synthesis and molecular properties of acceptor-substituted squaraine dyes. *Chem.—Eur. J. 19*, 218−232.

(25) Mayerhöffer, U., Fimmel, B., and Würthner, F. (2012) Bright near-infrared fluorophores based on squaraines by unexpected halogen effects. *Angew. Chem., Int. Ed. 124*, 168−171.

(26) Arun, K. T., Epe, B., and Ramaiah, D. (2002) Aggregation behavior of halogenated squaraine dyes in buffer, electrolytes, organized media, and DNA. *J. Phys. Chem. B 106*, 11622−11627.
(27) Jyothish, K., Hariharan, M., and Ramaiah, D. (2007) Chiral supramolecular assemblies of a squaraine dye in solution and thin films: concentration-, temperature-, and solvent-induced chirality inversion. *Chem.—Eur. J. 13*, 5944−5951.
(28) Ajayaghosh, A., Chithra, P., Varghese, R., and Divya, K. P. (2008) Controlled self-assembly of squaraines to 1D supramolecular architectures with high molar absorptivity. *Chem. Commun.*, 969−971.
(29) Chithra, P., Varghese, R., Divya, K. P., and Ajayaghosh, A. (2008) Solvent-induced aggregation and cation-controlled self-assembly of tripodal squaraine dyes: optical, chiroptical and morphological properties. *Chem.—Asian J. 3*, 1365−1373.
(30) Mayerhöffer, U., Deing, K., Gruß, K., Braunschweig, H., Meerholz, K., and Würthner, F. (2009) Outstanding short-circuit currents in BHJ solar cells based on NIR-absorbing acceptor-substituted squaraines. *Angew. Chem., Int. Ed. 48*, 8776−8779.
(31) Wang, L., Li, L. L., Fan, Y. S., and Wang, H. (2013) Host−guest supramolecular nanosystems for cancer diagnostics and therapeutics. *Adv. Mater. 25*, 3888−3898.
(32) Wang, L., Li, L. L., Ma, H. L., and Wang, H. (2013) Recent advances in biocompatible supramolecular assemblies for biomolecular detection and delivery. *Chin. Chem. Lett. 24*, 351−358.
(33) Xu, J. H., Gao, F. P., Liu, X. F., Zeng, Q., Guo, S. S., Tang, Z. Y., Zhao, X. Z., and Wang, H. (2013) Supramolecular gelatin nanoparticles as matrix metalloproteinase responsive cancer cell imaging probes. *Chem. Commun. 49*, 4462−4464.
(34) Wang, H., Wang, S., Su, H., Chen, K. J., Armijo, A. L., Lin, W. Y., Wang, Y., Sun, J., Kamei, K. I., Czernin, J., Radu, C. G., and Tseng, H. R. (2009) A supramolecular approach for preparation of size-controlled nanoparticles. *Angew. Chem., Int. Ed. 48*, 4344−4348.
(35) Chen, K. J., Wolahan, S. M., Wang, H., Hsu, C. H., Chang, H. W., Durazo, A., Hwang, L. P., Garcia, M. A., Jiang, Z. K., Wu, L., Lin, Y. Y., and Tseng, H. R. (2011) A small MRI contrast agent library of gadolinium(III)-encapsulated supramolecular nanoparticles for improved relaxivity and sensitivity. *Biomaterials 32*, 2160−2165.
(36) Zhang, D., Zhao, Y. X., Gao, Y. J., Gao, F. P., Fan, Y. S., Li, X. J., Duan, Z. Y., and Wang, H. (2013) Anti-bacterial and *in vivo* tumor treatment by reactive oxygen species generated by magnetic nanoparticles. *J. Mater. Chem. B 1*, 5100−5107.
(37) Wang, S., Chen, K. J., Wu, T. H., Wang, H., Lin, W. Y., Ohashi, M., Chiou, P. Y., and Tseng, H. R. (2010) Photothermal effects of supramolecularly assembled gold nanoparticles for the targeted treatment of cancer cells. *Angew. Chem., Int. Ed. 49*, 3777−3781.
(38) Fan, K., Cao, C., Pan, Y., Lu, D., Yang, D., Feng, J., Song, L., Liang, M., and Yan, X. (2012) Magnetoferritin nanoparticles for targeting and visualizing tumour tissues. *Nat. Nanotechnol. 7*, 459−464.
(39) Barreto, J. A., O'Malley, W., Kubeil, M., Graham, B., Stephan, H., and Spiccia, L. (2011) Nanomaterials: applications in cancer imaging and therapy. *Adv. Mater. 23*, H18−H40.
(40) Gabizon, A., and Papahadjopoulos, D. (1988) Liposome formulations with prolonged circulation time in blood and enhanced uptake by tumors. *Proc. Natl. Acad. Sci. U.S.A. 85*, 6949−6953.
(41) Mayerhöffer, U., and Würthner, F. (2012) Halogen−arene interactions assist in self-assembly of dyes. *Angew. Chem., Int. Ed. 51*, 5615−5619.
(42) Szoka, F., and Papahadjopoulos, D. (1978) Procedure for preparation of liposomes with large internal aqueous space and high capture by reverse-phase evaporation. *Proc. Natl. Acad. Sci. U.S.A. 75*, 4194−4198.
(43) Szoka, F., and Papahadjopoulos, D. (1980) Comparative properties and methods of preparation of lipid vesicles (liposomes). *Annu. Rev. Biophy. Bioeng. 9*, 467−508.
(44) Gao, F. P., Lin, Y. X., Li, L. L., Liu, Y., Mayerhöffer, U., Spenst, P., Su, J. G., Li, J. Y., Würthner, F., and Wang, H. (2014) Supramolecular adducts of squaraine and protein for noninvasive tumor imaging and photothermal therapy *in vivo*. *Biomaterials 35*, 1004−1014.
(45) Danielli, A., Favazza, C. P., Maslov, K., and Wang, L. V. (2010) Picosecond absorption relaxation measured with nanosecond laser photoacoustics. *Appl. Phys. Lett. 97*, 163701.
(46) Zeng, J., Goldfeld, D., and Xia, Y. (2013) A plasmon-assisted optofluidic (PAOF) system for measuring the photothermal conversion efficiencies of gold nanostructures and controlling an electrical switch. *Angew. Chem., Int. Ed. 52*, 4169−4173.
(47) Tian, Q., Jiang, F., Zou, R., Liu, Q., Chen, Z., Zhu, M., Yang, S., Wang, J., Wang, J., and Hu, J. (2011) Hydrophilic Cu9S5 nanocrystals: A photothermal agent with a 25.7% heat conversion efficiency for photothermal ablation of cancer cells in vivo. *ACS Nano 5*, 9761−9771.
(48) Berlier, J. E., Rothe, A., Buller, G., Bradford, J., Gray, D. R., Filanoski, B. J., Telford, W. G., Yue, S., Liu, J., Cheung, C. Y., Chang, W., Hirsch, J. D., Haugland, R. P., Beechem, J. M., and Haugland, R. P. (2003) Quantitative comparison of long-wavelength Alexa Fluor dyes to Cy dyes: fluorescence of the dyes and their bioconjugates. *J. Histochem. Cytochem. 51*, 1699−1712.
(49) Lee, N., Choi, S. H., and Hyeon, T. (2013) Nano-sized CT contrast agents. *Adv. Mater. 25*, 2641−2660.
(50) Hume, D. A. (2006) The mononuclear phagocyte system. *Curr. Opin. Immunol. 18*, 49−53.
(51) Ji, X., Dong, S., Wei, P., Xia, D., and Huang, F. (2013) A novel diblock copolymer with a supramolecular polymer block and a traditional polymer block: preparation, controllable self-assembly in water, and application in controlled release. *Adv. Mater. 25*, 5725−5729.